TuJnaS

Original Article

Thamar University Journal of Natural & Applied Sciences 10(2) (2025) 36– 46

DOI: https://doi.org/10.59167/tujnas.v10i2.3017

Investigation of Structural, Optical Characteristics, and Morphological Properties, as well as the Antibacterial Efficacy of MgO-$Bi_{2-x}Ag_xO_3$ Nanocomposites Synthesized via the Solvent-Deficient Method

Annas Al-Sharabi[1,*], Kholod Saleh Sada'a[1], Ahmed Al-Osta[1], Adnan Alnehia[1], Fawaz Al-Badai[2], Ahmed Saleh Alhajj[3], Abdulkarem Alrezaki[4], and Najeeb Al-Hijaini[1]

[1]Physics Department, Faculty of Applied Science, Thamar University, Dhamar 87246, Yemen.

[2]Biology Department, Faculty of Applied Science, Thamar University, Dhamar, 87246, Yemen.

[3]Department of Microbiology, Faculty of Veterinary Medicine, Thamar University, Dhamar 87246, Yemen.

[4]Biology Department, Faculty of Education, Thamar University, Dhamar, 87246, Yemen.

***Corresponding Author:** Annas Al-Sharabi, Physics Department, Faculty of Applied Science, Thamar University, Dhamar 87246, Yemen. E-mail: annas.alsharabi3@gmail.com

Received: 2 November 2025. Received (in revised form): 14 December 2025. Accepted: 17 December 2025. Published: 28 December 2025.

Abstract:

In this work, MgO–$Bi_{2-x}Ag_xO_3$ nanocomposites with different silver contents (x = 0.00, 0.03, 0.05, and 0.07) were synthesized using a simple solvent-deficient method. The structural, optical, morphological, and antibacterial properties of the prepared materials were systematically investigated. X-ray diffraction analysis confirmed that all samples crystallized in the monoclinic α-Bi_2O_3 phase, with no detectable secondary phases related to MgO or AgO, suggesting that these components were either highly dispersed or present in an amorphous form. The average crystallite size was found to increase with Ag content up to x = 0.05, followed by a slight decrease at x = 0.07. Scanning electron microscopy revealed agglomerated particles with relatively uniform distribution, while silver doping led to noticeable improvements in surface morphology. Energy-dispersive X-ray spectroscopy confirmed the presence of Mg, Bi, O, and Ag in compositions close to the intended stoichiometry. Optical studies based on UV–visible spectroscopy showed that the optical bandgap decreased slightly with increasing Ag content, with values of 3.14, 3.13, 3.10, and 3.11 eV for x = 0.00, 0.03, 0.05, and 0.07, respectively. These changes were attributed to the introduction of Ag-related impurity states within the band structure. The antibacterial activity of the nanocomposites was evaluated against both Gram-negative and Gram-positive bacteria using the disc diffusion method. Silver-doped samples exhibited enhanced antibacterial performance compared with the undoped material, with the highest activity observed for the Ag-containing nanocomposites. Notably, inhibition zones exceeding 23 mm were recorded against Gram-negative bacteria, highlighting the strong antibacterial effect associated with Ag incorporation. Overall, the results demonstrate that MgO–$Bi_{2-x}Ag_xO_3$ nanocomposites prepared by the solvent-deficient method possess promising structural, optical, and antibacterial properties, making them potential candidates for applications in medical and environmental fields.

Keywords: MgO–Bi_2O_3; silver doping; Structural properties; Optical bandgap; Antibacterial activity; Solvent-deficient method

1. Introduction

In recent years, nanomaterials have attracted considerable attention because of their unique physical and chemical properties, which differ markedly from those of their bulk counterparts [1, 2]. Owing to their reduced dimensions, high surface-to-volume ratio, and tunable surface characteristics, nanoparticles often exhibit enhanced optical, electrical, and antibacterial behaviors. These features make nanotechnology a powerful tool for improving the performance of inorganic materials, particularly in applications related to antimicrobial activity and environmental protection [2].

Magnesium oxide (MgO) is a wide-bandgap semiconductor that typically crystallizes in a cubic structure and exhibits high thermal and

chemical stability [3]. Mg ionic radii is 0.72 Å and it has +2 oxidation state [4, 5]. In its bulk form, MgO has a large bandgap of approximately 7.8 eV, which limits its direct application in optoelectronic devices. However, when reduced to the nanoscale, the bandgap decreases significantly, often reaching values around 5 eV, thereby improving its optical activity [6]. MgO nanoparticles are also known for their strong surface reactivity and catalytic properties, as well as their effectiveness against a broad range of Gram-positive and Gram-negative bacteria [7, 8]. Importantly, MgO shows relatively low toxicity toward mammalian cells compared with many other metal oxides, which makes it an attractive candidate for biomedical and pharmaceutical applications [9, 10]. As a result, increasing effort has been devoted to the synthesis of MgO-based nanoparticles and nanocomposites for advanced technological uses [11].

The antibacterial activity of MgO nanoparticles is commonly attributed to the generation of reactive oxygen species, particularly superoxide radicals. These species form when oxygen molecules interact with the nanoparticle surface and can disrupt bacterial cell membranes by damaging proteins and phospholipids, ultimately leading to cell death [12]. Despite these advantages, the optical response and antibacterial efficiency of MgO alone remain limited, motivating the development of composite systems that combine MgO with other functional oxides.

Bismuth oxide, also known as bismuth trioxide (Bi_2O_3), is a yellow chemical compound [5]. Bi_2O_3 is another material of significant interest due to its narrow bandgap and versatile physical properties. It exists in several polymorphic forms (α, β, γ, δ, ε, and ω), with the monoclinic α-Bi_2O_3 phase being the most stable at relatively low temperatures [13, 14]. Bi_2O_3 is a p-type semiconductor with a direct bandgap of approximately 2.85 eV, making it responsive to visible light [15, 16]. At the nanoscale, Bi_2O_3 exhibits notable photoluminescence, high dielectric permittivity, good ionic conductivity, and strong catalytic activity, while remaining largely non-toxic [17-20]. These characteristics have enabled its use in a wide range of applications, including gas sensors, optical coatings, photovoltaic devices, optoelectronics, and photocatalysis [21-24]. Moreover, Bi_2O_3 has demonstrated promising antibacterial activity, further expanding its potential utility [25-27].

Several studies have shown that combining Bi_2O_3 with other metal oxides can significantly improve its photocatalytic and antibacterial performance. For example, Bi_2O_3-MgO nanocomposites have been reported to exhibit narrower bandgap values and enhanced photocatalytic activity compared with either component alone [23]. Similar improvements have been observed in CeO_2–Bi_2O_3 and ZnO-Bi_2O_3 nanocomposites, where modifications in microstructure and charge-carrier dynamics led to improved optical and antibacterial behavior [28, 29]. These findings suggest that heterostructure formation plays a key role in tailoring material properties.

Silver nanoparticles have long been recognized for their strong antibacterial activity and relatively low toxicity to humans [30-32]. Owing to their size- and shape-dependent optical and electronic properties, Ag nanoparticles are also attractive for optoelectronic applications [33, 34]. Incorporating silver into metal oxide systems can introduce new electronic states, modify band structures, and enhance charge-carrier separation, which collectively improve optical absorption and antibacterial efficiency.

Based on these considerations, the present study focuses on the synthesis of MgO–$Bi_{2-x}Ag_xO_3$ nanocomposites (x = 0.00, 0.03, 0.05, and 0.07) using a simple and cost-effective solvent-deficient method. The structural, morphological, and optical properties of the synthesized nanocomposites were systematically investigated using X-ray diffraction, scanning electron microscopy, energy-dispersive X-ray spectroscopy, and UV–visible spectroscopy. In addition, the antibacterial activity of the materials was evaluated against both Gram-negative and Gram-positive bacterial strains using the disc diffusion method. The study aims to clarify the role of Ag incorporation in modifying the physical properties and antibacterial performance of MgO–Bi_2O_3-based nanocomposites, with a view toward potential medical and environmental applications.

2. Experimental procedure

2.1 Materials and Methods

The MgO-$Bi_{2-x}Ag_xO_3$ nanocomposites with several doping levels (x = 0, 0.03, 0.05, and 0.07) were fabricated using a straightforward solvent-deficient method. The chemicals used included $Bi(NO_3)_3{\cdot}5H_2O$, ≥ 98 %; Fluka, $Mg(NO_3)_2{\cdot}6H_2O$, $AgNO_3$, > 98.5%; Fluka-Garande, and $NaHCO_3$, > 98.5%; Fluka. All reagents were employed as received without any further purification. The overall reaction governing the synthesis process is abridged as follows:

$$(2\text{-}x)Bi(NO_3)_3{\cdot}5H_2O + Mg(NO_3)_2{\cdot}6H_2O + xAg(NO_3) + 8NaHCO_3 \rightarrow MgO\text{-}Bi_{(2-x)}Ag_xO_3 + (8\text{-}2x)NO_2 + (20\text{-}5x)\,H_2O + 4Na_2O + 8CO_2 + (2\text{-}x)O_2 \quad (1)$$

2.2 Preparation Process

To prepare the nanocomposites, stoichiometrically calculated amounts of $Bi(NO_3)_3{\cdot}5H_2O$, $Mg(NO_3)_2{\cdot}6H_2O$, and $AgNO_3$ were mixed with the appropriate amount of $NaHCO_3$. These components were then ground together for 20 minutes in a mortar at 23±1 °C. During the initial minutes, a degassing reaction occurred due to the release of CO_2, causing the slurry mixture to become more viscous. After drying the mixture overnight at 23 ± 1 °C, a dark powder was obtained. This powder was subsequently washed three times using distilled water and a filter flask. The cleaned powders were then heated in an oven at 773 K for two hours, with the temperature being adjusted at a rate of 10 K/min. Following this calcination step, the final powders were ground again using the mortar and pestle and then subjected to further characterization.

2.3 Antibacterial test

To evaluate the antibacterial efficacy of MgO-$Bi_{2-x}Ag_xO_3$ nanocomposites (x = 0, 0.03, 0.05, and 0.07), a disc diffusion method was employed against Gram-negative bacteria (*Salmonella typhimurium* and *Pseudomonas aeruginosa*) and Gram-positive bacteria (*Staphylococcus aureus*). Prior to testing, the bacterial strains were confirmed using biochemical assays. The nanocomposite samples were prepared by suspending them in sterile distilled water and creating four working dilutions from a stock solution of 50 mg/ml. These dilutions were utilized to impregnate sterile filter paper disks (6 mm diameter) at concentrations of 500, 250, 125, and 62.5 µg/disk (denoted as S_1, S_2, S_3, and S_4, respectively). Agar plates were injected with the bacterial cultures using swabs to form a bacterial lawn, after which the impregnated disks were placed on the surface. The plates were then incubated at 37 °C for 19-21 hours. Following incubation, the zones of inhibition (ZOI) around each disk were measured to the nearest millimeter(mm). A negative control utilizing distilled water (DW) was incorporated into the experimental setup to provide a baseline for comparison. This methodology allowed for the assessment of the antibacterial activities of the MgO–$Bi_{2-x}Ag_xO_3$ nanocomposites against the selected bacterial strains, facilitating a comprehensive evaluation of their potential as antimicrobial agents.

2.4 Characterization Techniques

The crystalline structure of the synthesized nanocomposites was examined using X-ray diffraction (XRD) utilizing an XD-2 X-ray diffractometer operating at 36 kV and 20 mA, sourced from China. X-ray diffraction was recorded with Cu Kα radiation (λ = 1.5406 Å). Diffraction patterns were recorded over a suitable 2θ range to identify phase composition and crystallinity. Average crystallite sizes were estimated using the Scherrer equation. Surface morphology and particle distribution were investigated using scanning electron microscopy (SEM). SEM was conducted using a JEOL-JSM 6360 LV instrument based in Tokyo, Japan, to investigate micro-structural features. Elemental composition and elemental mapping were analyzed by energy-dispersive X-ray spectroscopy (EDX) attached to the SEM: JEOL-JSM 6360 LV instrument. Optical properties were studied using UV–visible absorption spectroscopy in the wavelength range of 200–800 nm. The optical bandgap energies were estimated from Tauc plots by extrapolating the linear portion of $(\alpha h\nu)^2$ versus photon energy ($h\nu$). UV-visible spectra were obtained employing a SPECORD 200 spectrophotometer.

3. Results and discussion

3.1 XRD study

The XRD patterns of as-prepared MgO, α-Bi_2O_3, and MgO over Bi_2O_3 nanocomposite were discussed in our previous study [35]. The crystalline architecture and composition integrity of the synthesized MgO-Bi_2O_3 and Ag-doped MgO-Bi_2O_3 nanocomposites were emphasized through XRD analysis. The diffraction patterns were recorded over a 15° to 65° range, as depicted in Figure 1. The observed peaks aligned well with the JCPDS card number 00-041-1449 [36], corresponding to the monoclinic crystalline structure of α-Bi_2O_3 (space group P21/c), with the (120) peak being the most prominent. No MgO peaks were detected due to its minimal presence

in the nanocomposite and the significant dispersion of MgO particles. However, the presence of MgO was validated through the EDX spectrum. The ionic radius of Bi^{+3} (coordination number = 6) is 1.03 Å, whereas that of Mg^{+2} (coordination number = 6) is only 0.72 Å.

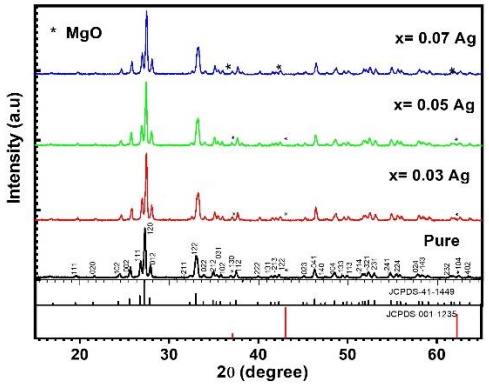

Figure 1: X-ray diffraction patterns of MgO–$Bi_{2-x}Ag_xO_3$ nanocomposites with different Ag contents (x = 0.00, 0.03, 0.05, and 0.07), confirming the monoclinic α-Bi_2O_3 phase.

The results suggest that MgO has an amorphous nature in the samples and/or is highly dispersed on Bi_2O_3 [23]. Therefore, it can be deduced that the existence of MgO suppressed the growth of the Bi_2O_3 crystals. The addition of Mg^{+2} into the Bi_2O_3 lattice led to a change in the cell parameters of the monoclinic phase. Conversely, the existence of Bi_2O_3 appeared to impede the crystallization of MgO [23]. No diffraction peaks were observed besides those of Bi_2O_3, indicating the absence of crystallographic phase impurities in the pure MgO-Bi_2O_3 and Ag-doped MgO-Bi_2O_3 nanocomposites. No peak relating to diffraction from MgO and AgO phases could be identified for x = 0.03, 0.05, and 0.07, indicating that the structure is not disturbed by Ag doping.

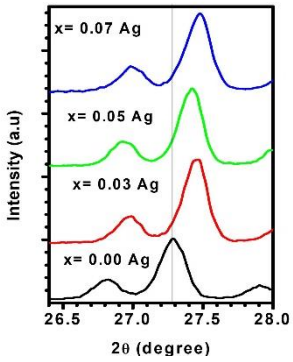

Figure 2: XRD patterns showing a slight peak shift toward the higher angle 2θ of MgO-$Bi_{2-x}Ag_xO_3$ nanocomposites (x = 0.0, 0.03, 0.05, and 0.07).

The intensity of the predominant peak was increased for Ag-doped MgO-Bi_2O_3 nanocomposites as compared to pure MgO-Bi_2O_3 nanocomposites and the diffraction peak shifts towards a higher angle. As observed in Figure 2 at (x = 0.00, 0.03, 0.05, and 0.07), the diffraction pattern of nanocomposites is shifted to a small extent with slight changes in the lattice as compared to pure Bi_2O_3 nanoparticles (The pattern corresponds to monoclinic structure, matching well with JCPDS card number 00-041-1449 for α-Bi_2O_3) indicating the increase in interplanar spacing of MgO-Bi_2O_3 [35]. This might be due to inserting the Ag^{+1} ions in the composite. It indicates Bi^{+3} ions have been successfully substituted by the dopant ions. This is possible because of the closeness in the ionic radii between Bi (1.03 Å) and Ag (1.15 Å), which is more suitable or preferred. Accordingly, oxygen vacancy will be generated to favor the structure reorganization and keep an overall neutral charge after Bi^{+3} in MgO-Bi_2O_3 crystal is replaced by property Ag^{+1} [37-39].

The constants of lattice a, b, and c for the monoclinic phase of α-Bi_2O_3 were computed via the equations:

$$\frac{1}{d^2} = \frac{1}{sin^2\beta}\left(\frac{h^2}{a^2} + \frac{k^2 sin^2\beta}{b^2} + \frac{l^2}{c^2} - \frac{2hl\, cos\beta}{ac}\right) \quad (2)$$

Here, d represents the interplanar distance, while h, k, and l denote the Miller indices. The volume (V) of the unit cell in monoclinic structures was computed from $V = abc \times sin\ \beta$ and given in Table 1. The density (ρ) and d-spacing for monoclinic structures were measured by utilizing the equation: $\rho = (Z \times M)/(N \times a^3)\ g\,.cm^{-3}$ [35] (where M is the molecular weight (g/mol) of the crystal, Z is the number of molecules in a unit cell. V is the volume of the crystalline unit cell, and N is Avogadro's number) and $2dsin\theta = n\lambda$ (where 'd' is the inter-planar spacing of a particular set of crystal plane, 'λ' is the wavelength of the incident X-ray, in our case the wavelength used is that of copper (λ = 1.5407 Å), θ is the diffraction angle, and 'n' is the order of diffraction) [40]. It was observed that the lattice's constant values are approximated to the values of the standard lattice constants. Calculated theoretical density, volume, and interplanar distance (d) between the crystal planes, at major peaks corresponding to the (120) for Bi_2O_3 planes, are in agreement with the standard values. It can be said that the dominant peak angle shifts, the change in d value, and the lattice constants are caused by the Ag^{+1} dopant [39]. It shows a slight change in lattice parameters. The increase in the unit cell volume of MgO-Bi_2O_3 nanocomposite was observed, showing shrinkage in the unit cell as compared to pure α-Bi_2O_3. The unit cell volume and the lattice constant (c) of MgO-$Bi_{(2-x)}Ag_xO_3$ nanocomposites at x = 0.03, 0.05, and 0.07, the phase in the nanocomposite is increased as compared to pure α-Bi_2O_3 (x = 0.00). A slight peak shift toward the higher angle 2θ (Figure 2) and the change in d value and unit cell volume are evidence of the incorporation of Ag ions. The reduction in lattice parameters (a, b) suggests that compressive strain has been introduced into the lattice. Shifts in peak angles and lattice strain can lead to changes in the crystallographic planes (d-spacing). However, the observed changes in lattice constant and unit cell volume with increasing Ag-doping concentration can be attributed to the ionic radius differences between Ag^{+1} and Bi^{+3} ions, as the ionic radius of Ag^{+1} (1.15 Å) is larger than that of Bi^{+3} (1.03 Å). Scherrer's equation was utilized to evaluate the average crystallite size (D) and micro-strain (ε) via XRD data of MgO-$Bi_{2-x}Ag_xO_3$ nanocomposites (x = 0.0, 0.03, 0.05, and 0.07), given as [41]:

$$D = 0.9\lambda/(\varphi\, cos\theta) \quad (3)$$

$$\varepsilon = \varphi/(4\, tan\theta) \quad (4)$$

where φ is the full width at half maximum (FWHM), θ is the angle of the peak maximum, and λ is the CuK_α wavelength (λ = 1.5406 Å) from the XRD calculations given in Table 2. The dislocation density(δ) due to crystal imperfections was estimated by utilizing the equation: $\delta = 1/D^2$, and the evaluated values are recorded in Table 2. The inverse relationship between the dislocation density (δ) and grain size indicates a reduction in the crystallite size due to the large dislocation density value [42].

Table 1: Structural parameters of MgO-$Bi_{2-x}Ag_xO_3$ nanocomposites (x = 0.0, 0.03, 0.05 and 0.07).

Oxides	Oxides	*a* (Å)	*b* (Å)	*c* (Å)	Volume (Å³)	Density (g/cm³)	d-spacing (Å)
JCPDS 011-345	MgO	4.203	-	-	74.25	3.56	2.42
JCPDS 014-1449	Bi_2O_3	5.849	8.169	7.512	330.52	9.36	3.255
***x* = 0.0**	Bi_2O_3 (120)	5.872	8.227	7.363	326.150	9.489	3.266
x = 0.03	Bi_2O_3 (120)	5.845	8.229	7.544	333.751	9.274	3.247
***x* = 0.05**	Bi_2O_3 (120)	5.841	8.202	7.558	333.143	9.290	3.251
***x* = 0.07**	Bi_2O_3 (120)	5.843	8.195	7.541	332.204	9.317	3.245

Table 2: The D, ε, and δ evaluated from Scherrer's equation for $MgO\text{-}Bi_{2-x}Ag_xO_3$ nanocomposites (x = 0, 0.03, 0.05 and 0.07).

Oxides Individual	Oxides	D (nm)	$\varepsilon\times10^{-3}$	$\delta\times10^{-4}$ (nm^{-2})
x = 0.0	Bi_2O_3 (120)	36.07	4.07	7.69
x = 0.03	Bi_2O_3 (120)	38.54	3.79	6.73
x = 0.05	Bi_2O_3 (120)	39.74	3.68	6.33
x = 0.07	Bi_2O_3 (120)	39.32	3.70	6.31

The crystallite size (D) of $MgO\text{-}Bi_{2-x}Ag_xO_3$ nanocomposites (x = 0, 0.03, 0.05, and 0.07) were increasing with increasing Ag concentration, then decreased at x = 0.07. This indicates that Ag ions doped into the host matrix were strongly capped. Increase the average crystalline size, ascribed to the diffraction peaks of $MgO\text{-}Bi_2O_3$ shift towards higher 2θ values with an increase in the Ag concentration, which is due to Ag^{+1} (1.15 Å) ions that can uniformly substitute into the Bi^{+3} (1.03 Å) ions' sites or interstitial sites in the $MgO\text{-}Bi_2O_3$ lattice [43].

In case of substitution and due to the different ionic radii (Ag = 1.15 Å larger than Bi = 1.03 Å), a lattice distortion occurs, and this distortion increases with the increase in Ag concentration[43]. The δ was increased with a decrease in crystallite size and vice versa. Microstrain was found to be compressive and decreased with the silver doping. The microstrain and dislocation density will have an important effect on the optical parameters of the samples [42].

3.2. SEM and EDX Analysis

The SEM images in Figure 3 were utilized to analyze the morphology of $MgO\text{-}Bi_2O_3$ and $MgO\text{-}Bi_{(1.93)}Ag_{0.07}O_3$. The surface of the $MgO\text{-}Bi_2O_3$ sample appeared more agglomerated and irregular in shape, exhibiting significant roughness. In contrast, the Ag-doped sample exhibited a smoother surface with reduced agglomeration, suggesting improved morphology. Some of the nanoparticles appeared spherical; however, they also exhibited variations in shape and irregularity. These changes in surface characteristics were attributed to the influence of silver doping, which enhanced particle interaction and fusion, leading to a more uniform distribution and a decrease in overall surface roughness [44]. The development of uniform, minimal-agglomerated spheres is due to homogeneous nucleation during heating. In contrast, the formation of larger particles and a wider distribution may be due to varied heating zones [45-47]. The chemical compositions of the as-prepared nanocomposite were analyzed by energy-dispersive X-ray spectroscopy (EDX). It was performed to confirm the presence of Ag-ion in MgO/Bi_2O_3 crystal lattice. Figure 4 presents the EDX spectra of the pure MgO/Bi_2O_3 nanocomposite. The results clearly indicate the presence of the elements Bi, Mg, and O as the respective peaks are clearly visible. Moreover, the atomic percentages of Bi, Mg, and O are 88.7%, 0.4% and 10.9% respectively. In addition, EDX spectra of 0.07 for Ag-doped MgO/Bi_2O_3 sample are displayed in Figure 5.5b. Spectra reveal that only four elements, Bi, Mg, Ag, and O, exist in Ag-doped MgO/Bi_2O_3 nanocomposite with their weight percentage of 86.1 %, 0.5 %, 1.8 % and 11.6 % respectively, which indicates the doped Ag ions have entered into the lattice of $MgO/Bi_{(2-x)}Ag_xO_3$ nanocomposite. This also agrees with the foregoing XRD results.

3.3 Optical analysis

3.3.1 Optical Absorption and Transmission Spectra Study

Figure 5 presents the optical absorption spectra of the $MgO\text{-}Bi_{2-x}Ag_xO_3$ nanocomposites for various concentrations (x = 0, 0.03, 0.05, and 0.07). The pure $MgO\text{-}Bi_{2-x}Ag_xO_3$ nanocomposite (x = 0.00) exhibited a broad absorption band at 363 nm. Conversely, at x = 0.03, 0.05, and 0.07, distinct peaks appeared at 365, 367, and 369 nm, respectively. The primary absorption edge shifted towards longer wavelengths with increasing Ag doping. This overall trend suggests a red shift near the band edge with Ag incorporation. This shift in absorption can be attributed to the potential substitution of Bi ions with Ag ions within the crystal lattice or the mutual exchange of these ions. Additionally, the reduced absorption in the UV and near-visible regions can be attributed to the increased surface roughness caused by higher concentrations of Ag nanoparticles, which enhances scattering and reduces the intensity of incident light [48]. The peak intensity at 363 nm decreased as the Ag doping concentration increased, likely due to the reduced solubility of the highly doped $MgO\text{-}Bi_2O_3$ nanocomposites in solvents compared to the undoped counterparts.

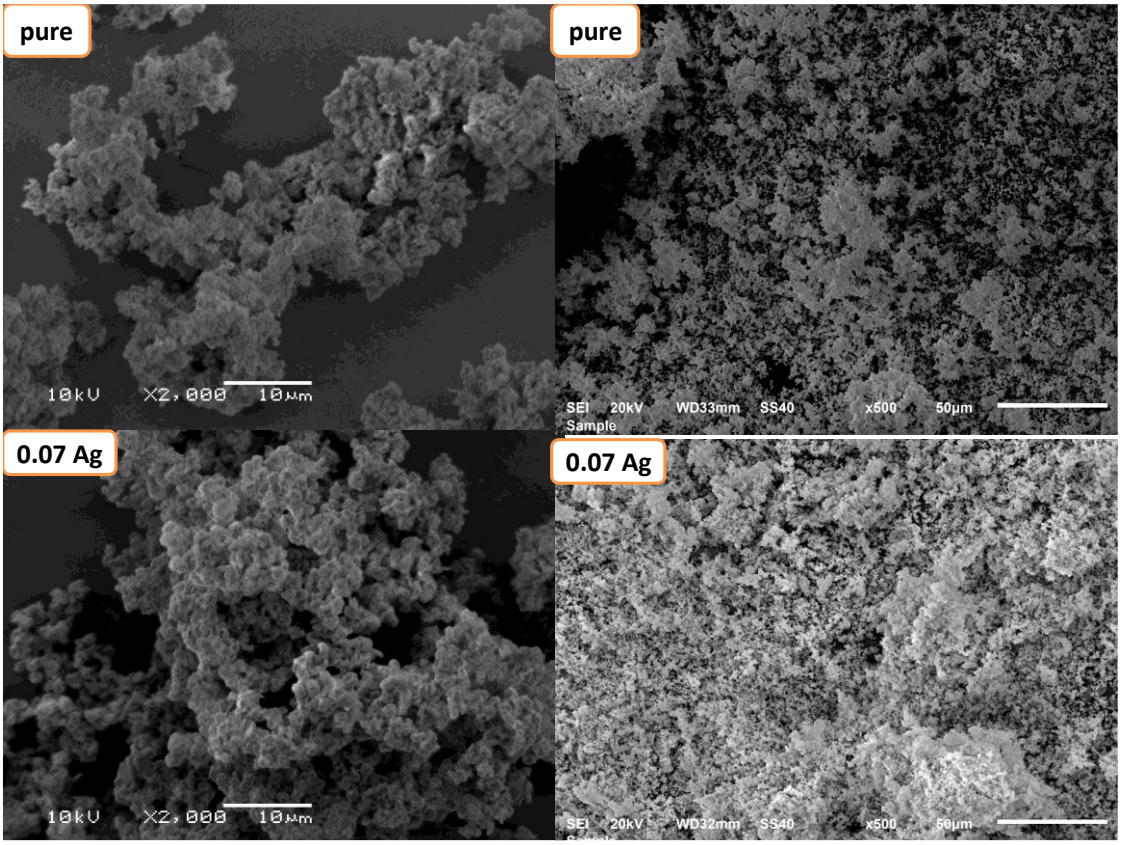

Figure 3: SEM micrographs of $MgO\text{–}Bi_{2-x}Ag_xO_3$ nanocomposites showing surface morphology and particle agglomeration as a function of Ag content.

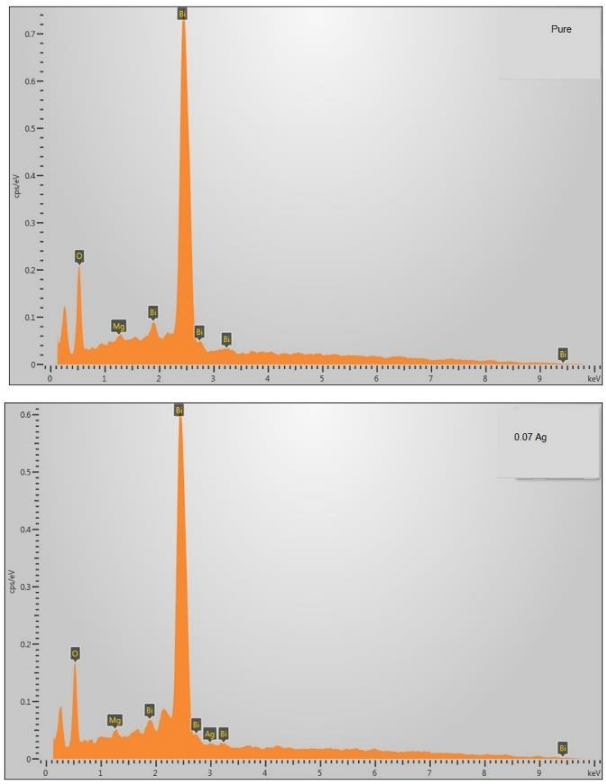

Figure 4: EDX spectra of MgO–$Bi_{2-x}Ag_xO_3$ nanocomposites illustrating the presence of Bi, Mg, O, and Ag elements.

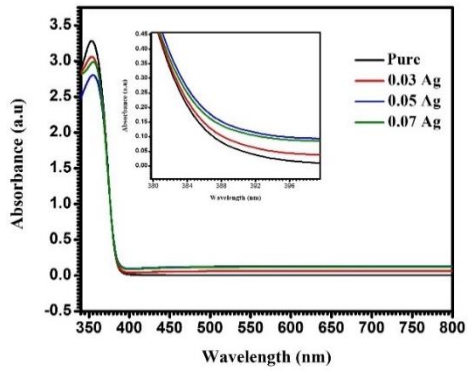

Figure 5: UV–visible absorption spectra of MgO–$Bi_{2-x}Ag_xO_3$ nanocomposites with varying Ag concentrations.

The transmittance (T) measurements for MgO-$Bi_{2-x}Ag_xO_3$ nanocomposites (x = 0, 0.03, 0.05, and 0.07) as a function of wavelength (λ) are depicted in Figure 6. It was observed that T exhibited high values across most measured wavelengths. The nanocomposites demonstrated significant visible-range transmittance, making them suitable candidates for transparent window materials in optoelectronic devices. The optical transmittance values were 99%, 91%, 80%, and 82% for the respective samples, indicating a decrease in the UV and near-visible regions for all samples, with the highest transmittance at x = 0.00. This is attributed to the absence of free electrons (i.e., electrons are bound to atoms via covalent bonds), necessitating a high-energy photon to break the electron linkage and move it to the conduction band [49].

The transmittance in the visible range decreased with increasing Ag^{+1} doping percentage. This reduction in optical transmission can be attributed to increased scattering caused by the surface roughness of the nanocomposites and the presence of oxygen vacancies. It is hypothesized that aggregation and agglomeration decrease grain size with increasing Ag content, further reducing transmittance. The work function of Ag, located between the valence band and conduction band of MgO-Bi_2O_3, enhances the light absorption capability of MgO-Bi_2O_3. The strong interaction between Ag and light arises from the conduction electrons on the Ag surface, which generate surface plasmon resonance (SPR) at specific wavelengths. This SPR phenomenon results in significant scattering and absorption of light [50].

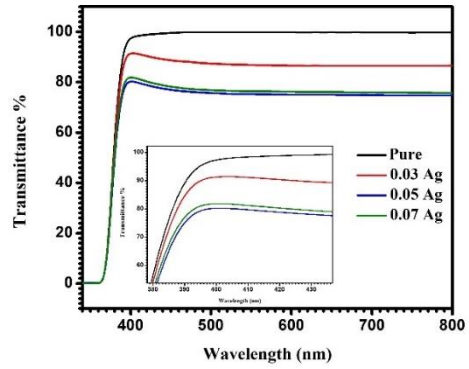

Figure 6: Transmittance as a function of wavelength of MgO-$Bi_{2-x}Ag_xO_3$ nanocomposites (x = 0, 0.03, 0.05, and 0.07).

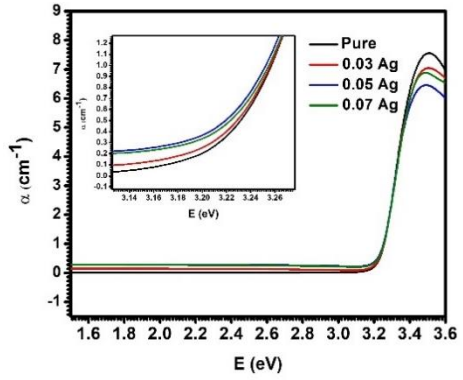

Figure 7: The absorption coefficient versus photon energy of MgO-$Bi_{2-x}Ag_xO_3$ nanocomposites (x = 0.0, 0.03, 0.05, 0.07).

The graph in Figure 7 illustrates the absorption coefficient (α) plotted against the photon energy (E) of the incident light. By establishing a fundamental connection between transmittance (T) and photon absorbance (A), the absorption coefficient (α) was constrained, offering insights into the nature of electron transitions. The calculation of α was based on Lambert's formula [51], as depicted below.

$$I = I_o\, e^{-\alpha t} \qquad (5)$$

where I is the instantaneous photon intensity, Io is the initial photon intensity, and t is the thickness of the cuvette. The α can be computed by utilizing the following equation:

$$\alpha(\lambda) = \left(\frac{1}{t}\right)\left(ln\,\frac{I_o}{I}\right) = \left(\frac{1}{t}\right)\left(ln\,\frac{1}{T}\right) = \frac{2.303\,A}{t} \qquad (6)$$

The variation of α(λ) for MgO-$Bi_{2-x}Ag_xO_3$ nanocomposites (x = 0, 0.03, 0.05 and 0.07) with photon energy is illustrated in Figure 7. The α of both pure and Ag-doped MgO-Bi_2O_3 nanocomposites increased with higher concentrations of Ag nanoparticles. This increase is attributed to the rise in the number of charge carriers, which in turn enhances absorbance and the α of MgO-$Bi_{2-x}Ag_xO_3$ nanocomposites [52-54].

At lower photon energies, absorption is minimal, indicating a reduced possibility of electron transitions because the incident photon energy is insufficient to promote electrons from the valence band (VB) to the conduction band (CB) (hυ < Eg). Conversely, at higher energies, the absorption is more significant, demonstrating a greater probability for electron transitions as the incident photon energy becomes sufficient to move electrons from the valence band to the conduction band. This indicates that the incident photon energy exceeds the forbidden energy gap [49]. A continuous increase in α with increasing E is observed across the entire measured photon energy range (3.1–3.3 eV), with the increase becoming more rapid near the material's optical bandgap energy. The highest absorption coefficient was noted for the sample with 0.05 Ag. Additionally, it was observed that reducing the size of nanoparticles decreases the absorption coefficient in the samples.

3.3.2 Optical Bandgap (E_g) Determination

The optical bandgap (Eg) can be determined using the Tauc plot approach, which correlates the incident light frequency (υ) with the photon energy (hυ) based on the equation [55]:

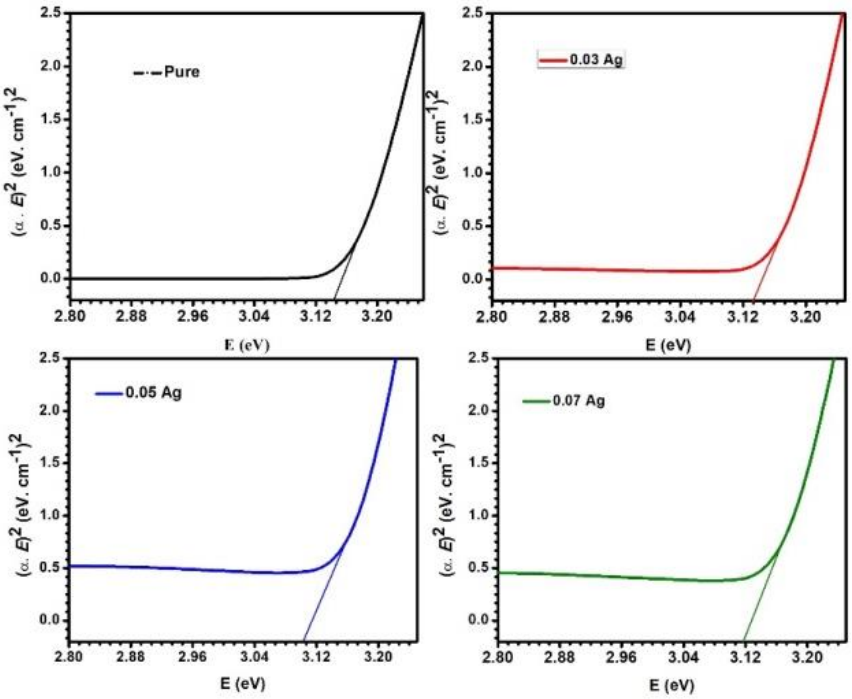

Figure 8: Tauc plots used to estimate the optical bandgap energies of MgO–$Bi_{2-x}Ag_xO_3$ nanocomposites.

$$(\alpha.\, h\upsilon)^n = A\left(h\upsilon - E_g\right) \quad (7)$$

where ν represents the incident light frequency, h is Planck's constant, A is a constant linked to the effective masses of electrons and holes in the material, and n varies depending on the type of electronic transition. For a direct allowed transition, n can be 1/2, for an allowed indirect transition, n is 2, for a forbidden direct transition, n is 3/2, and for a forbidden indirect transition, n is 3[55].

Bandgap energy (Eg) is a crucial parameter to evaluate a material's optical absorption performance. To determine Eg, the plot of $(\alpha h\upsilon)^2$ (for direct transitions) against hν is generated, and the linear portion of these plots is extrapolated to the hυ axis to derive the values of the optical direct bandgap Eg for the samples, as shown in Figure 8.

Direct transition E_g values were obtained for MgO-$Bi_{2-x}Ag_xO_3$ nanocomposites (x = 0, 0.03, 0.05, and 0.07) are listed in Table 3. The change in the bandgap value depends on many parameters, for example, carrier concentration, crystallite size, and the positions of the Ag dopant in the MgO-Bi_2O_3 lattice [56].

Table 3: The band gap values for MgO-$Bi_{2-x}Ag_xO_3$ nanocomposites (x = 0, 0.03, 0.05, and 0.07).

Oxides Individual	Band gap E_g (eV)
***x* = 0**	3.14
x = 0.03 Ag	3.13
***x* = 0.05 Ag**	3.10
***x* = 0.07 Ag**	3.11

The reduction in the bandgap (Eg) with increasing Ag^{+1} content corresponds to a red shift in the λ cut-off. This phenomenon is attributed to the formation of intermediate states between the conduction and valence bands of the MgO-Bi_2O_3 host matrix upon the addition of Ag. These intermediate states are responsible for the reduction in the bandgap of Ag–MgO-Bi_2O_3 nanocomposites. When Ag^{+1} is introduced into MgO-Bi_2O_3, defect states are generated below the conduction band, leading to a decrease in the bandgap. Ag^{+1} ions can be incorporated into the MgO-Bi_2O_3 lattice either by substituting Bi^{+3} ions, resulting in double ionized oxygen vacancies, or by occupying interstitial sites (Ag). The presence of silver impurities in MgO-Bi_2O_3 introduces an extra band within the energy gap, characteristic of a p-type material. This makes Ag act as an acceptor material, altering the bandgap of MgO-Bi_2O_3 nanocomposites and thereby reducing it. In contrast, donor materials exhibit a blue shift and an increase in the bandgap [57]. Consequently, doping MgO-Bi_2O_3 nanocomposites with silver can be advantageous for applications in optoelectronic devices due to the tunable energy bandgap values of the MgO-Bi_2O_3 nanocomposites [58].

3.3.3 Refractive Index(n) and Extinction Coefficient(k)

The α and incident photon wavelength (λ) can be utilized to evaluate the k, given as [59]:

$$k = \frac{\alpha\lambda}{4\pi} \quad (8)$$

Refractive index (n) is an important parameter of optical materials. Refractive index (n) can be given via the equation [59]:

$$n = \frac{1+R^2}{1-R^2} \quad (9)$$

where R is the reflection. Figure 9 (a and b) illustrates the behavior of n and k with the incident photon wavelength for MgO-$Bi_{2-x}Ag_xO_3$ nanocomposites (x = 0, 0.03, 0.05, and 0.07).

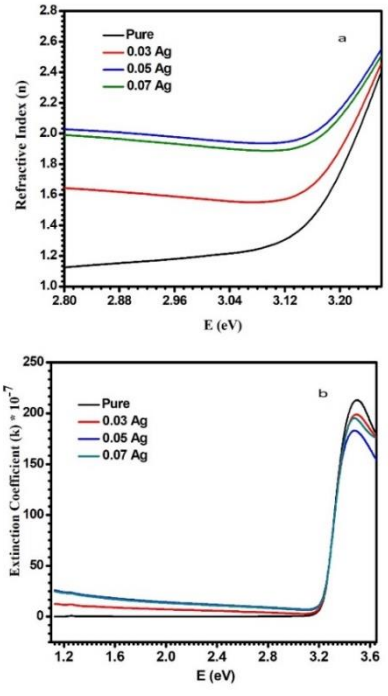

Figure 9: (a) Refractive index and (b) Extinction coefficient versus wavelength of MgO-$Bi_{2-x}Ag_xO_3$ nanocomposites (x = 0, 0.03, 0.05, and 0.07).

The refractive index (n) of MgO-Bi_2O_3 nanocomposites increases with the addition of Ag doping. This increase can be attributed to the rise in the number of free electrons and the consequent improvement in the surface of the nanocomposites, accompanied by a reduction in porosity [60]. Additionally, the increased refractive index with higher Ag doping levels may be due to lattice distortion and structural disorder within the nanocomposites. As illustrated in Figure 9a, the refractive index remains constant with increasing photon energy up to approximately 3.1 eV, after which it increases across all samples with varying Ag concentrations. Notably, the pure MgO-Bi_2O_3 nanocomposite shows a lower refractive index.

Figure 9b illustrates the k as a function of photon energy for all the samples investigated. The calculated extinction coefficient values increase with higher weight percentages of Ag. This coefficient emerges from light absorption when the photon wavelength is greater than or equal to the grain size. The likelihood of grain scattering increases with higher Ag doping, attributed to the enhancement in grain size and density of the nanocomposites. The non-zero extinction coefficient indicates the presence of additional transitions alongside the fundamental transition, suggesting that Ag doping modifies the structure of the host nanocomposites [52].

3.3.4 Optical Conductivity

The number of free charges in a material is termed optical conductivity (σ_{opt}). The σ_{opt} for any material can be expressed as [41]:

$$\sigma_{opt} = \frac{\alpha n c}{4\pi} \quad (10)$$

Here, c represents the velocity of light. Figure 10a illustrates the change of σ_{opt} with photon energy for all the samples. The values of σ_{opt} remained constant as the photon energy increased until approximately 3.1 eV, after which they increased, as shown in Figure 10a. This increase is attributed to variations in the α. The number of free carriers increases with higher Ag^{+1} content. The rise in optical conductivity is due to the creation of new levels within the bandgap, facilitating the movement of carrier charges from the valence band (VB) to the conduction band (CB). Consequently, this leads to a reduction in the bandgap and an increase in conductivity [61, 62].

3.3.5 Dielectric Constant

The real part (ε_r) of the dielectric constant represents a material's capacity to reduce the speed of light and can be computed via the equation:

$$\varepsilon_r = n^2 - k^2 \quad (11)$$

The component of the dielectric constant represented by the imaginary part (ε_i) characterizes the energy absorption resulting from dipole movement within an electric field. To determine (ε_i), the following relation can be used [59]:

$$\varepsilon_i = 2nk \quad (12)$$

The ratio of the ε_i to the ε_r of the dielectric constant yields insights into the loss factor:

$$\tan\delta = \frac{\varepsilon_i}{\varepsilon_r} \quad (13)$$

Figures 10b, 10c, and 10d illustrate the variations in the ε_r and ε_i parts of the dielectric constant, as well as the loss factor, with respect to photon energy. It is evident that the ε_r of the dielectric constant is primarily proportional to the square of the refractive index and therefore increases with the addition of Ag. The imaginary part of the dielectric constant is proportional to the k, as shown in relation (12), and it also increases with higher concentrations of Ag nanoparticles. The results obtained from measurements of the dielectric constant and loss angle show a close correlation with the optical energy gap of the studied materials. It was observed that increasing the doping concentration leads to an increase in the crystallite size calculated from X-ray diffraction (XRD) data. This increase in crystallite size may enhance polarization within the material, thereby increasing the dielectric constant. On the other hand, UV-Vis spectroscopic measurements indicate that the optical energy gap decreases with increasing doping concentration. This reduction in the optical energy gap may facilitate the movement of charge carriers, contributing to an increase in the loss factor. Therefore, the relationship between these properties suggests that modifications in the chemical composition significantly affect the electrical and optical properties of the material [63, 64].

The X-ray diffraction analysis revealed that the nanocomposites exhibited diffraction patterns characteristic of the monoclinic α-Bi_2O_3 phase, with no distinct peaks indicating the presence of MgO or AgO compounds. This suggests that the MgO and AgO phases are either amorphous or highly dispersed within the Bi_2O_3 matrix. The average crystallite size ranged from 36.07 to 39.74 nm, showing an increase with silver concentration, peaking at 0.05, followed by a decrease at 0.07. This trend can be attributed to the substitution of Bi+3 ions by Ag+ ions, which have a larger ionic radius. The increase in crystallite size with increasing silver doping concentration up to 0.05 can be attributed to the enhanced crystallinity of the samples resulting from the incorporation of Ag^+ ions into the Bi_2O_3 lattice. However, at higher silver concentration (x = 0.07), the decrease in crystallite size may be due to the formation of defects or lattice strain caused by the excess Ag^+ ions [65].

The optical properties assessed by UV-visible absorption spectroscopy indicated bandgap energies of 3.14, 3.13, 3.10, and 3.11 eV for silver doping concentrations of 0.00, 0.03, 0.05, and 0.07, respectively. The decrease in bandgap energy with increasing silver concentration can be attributed to the introduction of impurity levels within the bandgap, resulting from the substitution of Bi^{+3} ions by Ag^+ ions. However, at higher silver concentration

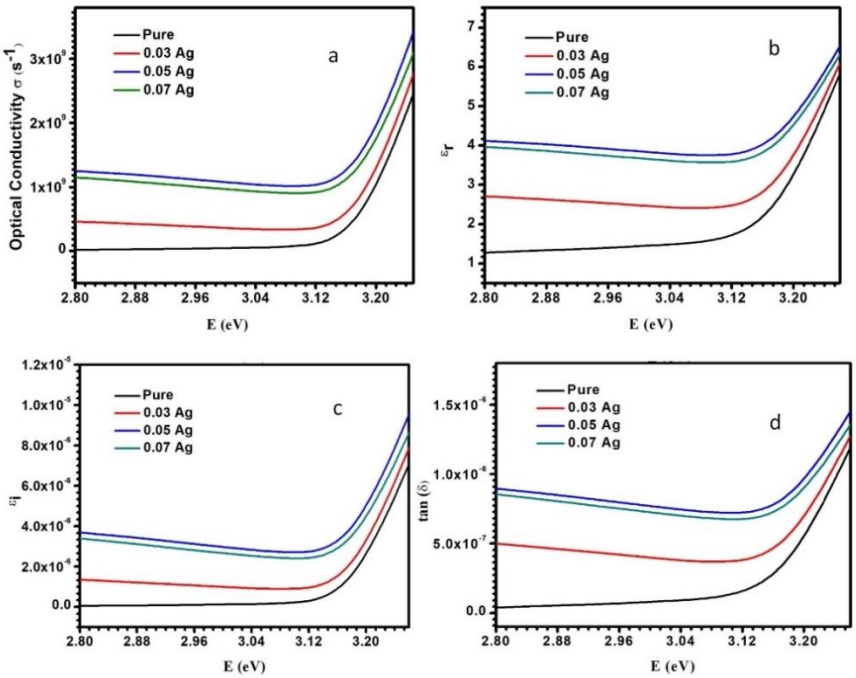

Figure 10: The change of (a) optical conductivity, (b) real dielectric constant, (c) imaginary dielectric constant, and (d) loss factor as a function of E(eV) for the synthesized samples

can be attributed to the introduction of impurity levels within the bandgap, resulting from the substitution of Bi^{+3} ions by Ag^{+} ions. However, at higher silver concentration (x = 0.07), the slight increase in bandgap energy may be due to the Burstein-Moss effect, where the excess Ag^{+} ions lead to a shift in the Fermi level and an increase in the bandgap energy [66].

3.4 Antibacterial activity

The antibacterial activity for MgO-$Bi_{(2-x)}Ag_xO_3$ nanocomposites (x = 0, 0.03, 0.05, and 0.07) were evaluated against gram-negative bacteria (*S. typhimurium and P. aeruginosa*) and gram-positive bacteria (*S. aureus*) (Table 4). Images of antibacterial studies on nanocomposites against bacterial pathogens are shown in Figure 11.

Table 4: Assessment of Antibacterial Efficacy of MgO-$Bi_{2-x}Ag_xO_3$ nanocomposites (x = 0, 0.03, 0.05, and 0.07).

Bacteria	Type of bacteria	ZOI (mm) at concentration in (µg/mL)				
		Con.	Pure	0.03 Ag	0.05 Ag	0.07 Ag
S. typhimurium	Negative	A1	15	20	18	20
		A2	15	19	17	19
		A3	15	18	16	18
		A4	15	17	16	19
P. aeruginosa	Negative	A1	14	21	21	23
		A2	13	18	20	18
		A3	14	18	18	19
		A4	15	19	17	18
S. aureus	Positive	A1	9	10	7	10
		A2	8	11	-	8
		A3	8	11	-	9
		A4	11	11	7	9

The antibacterial activity was determined by measuring the ZOI around the disc using the antibiotic zone scale (mm). The pure sample (at x = 0) nanocomposite has shown greater than 6 mm of inhibition against different types of bacteria. The addition of Ag content (x > 0) leads to an increase in the inhibitory activity of MgO-$Bi_{(2-x)}Ag_xO_3$ nanocomposites against several types of bacteria. This suggests that the growth inhibition ability of MgO-$Bi_{(2-x)}Ag_xO_3$ nanocomposites (x = 0, 0.03, 0.05, and 0.07) against both gram-negative and gram-positive bacteria have been significantly enhanced at the same concentration and growth conditions. The particle size (D) decreased as the doped concentration Ag^{+1}), the small size of the fabricated MgO-$Bi_{(2-x)}Ag_xO_3$ nanocomposites (x = 0.00, 0.03, 0.05, and 0.07) play an important role in their activity upon testing the gram-negative pathogen [67, 68]. MgO-$Bi_{(2-x)}Ag_xO_3$ nanocomposites (0.07) displayed the best antibacterial activity of both gram-negative and gram-positive bacteria, as depicted in Figure 11. The most significant effect of nanocomposites was found for the concentration (500 µg/disc) for all samples against the different types of bacteria. The results illustrated a higher ZOI for all fabricated materials (between 7 and 23 mm).

It is important to highlight that the MgO-$Bi_{(2-x)}Ag_xO_3$ nanocomposites prepared (x = 0, 0.03, 0.05, and 0.07) exhibited greater efficacy against gram-negative bacteria compared to gram-positive bacteria, potentially attributed to variations in bacterial cell structures. A thick lipopolysaccharide cell membrane characterizes gram-positive bacteria [69-71]. The differing antibacterial performance of the developed materials at varying Ag concentrations may be linked to surface defects. The inclusion of heavy metal ions, such as Bi^{+3}, Mg^{+2}, and Ag^{+1}, enhances antibacterial activity. These ions are drawn to the cell membrane through interactions with the thiol group (–SH) found in proteins on the external surface of the cell membrane. This attraction results in the penetration of metallic ions into the cell membrane, leading to protein denaturation and, in turn, damage to the bacterial cell membrane. Additionally, the surface characteristics of the nanocomposite contribute to mechanical disruptions in the membrane [72-77]. Table 5 shows a comparison of antibacterial analysis of MgO-$Bi_{(2-x)}Ag_xO_3$ nanocomposites with other previous studies.

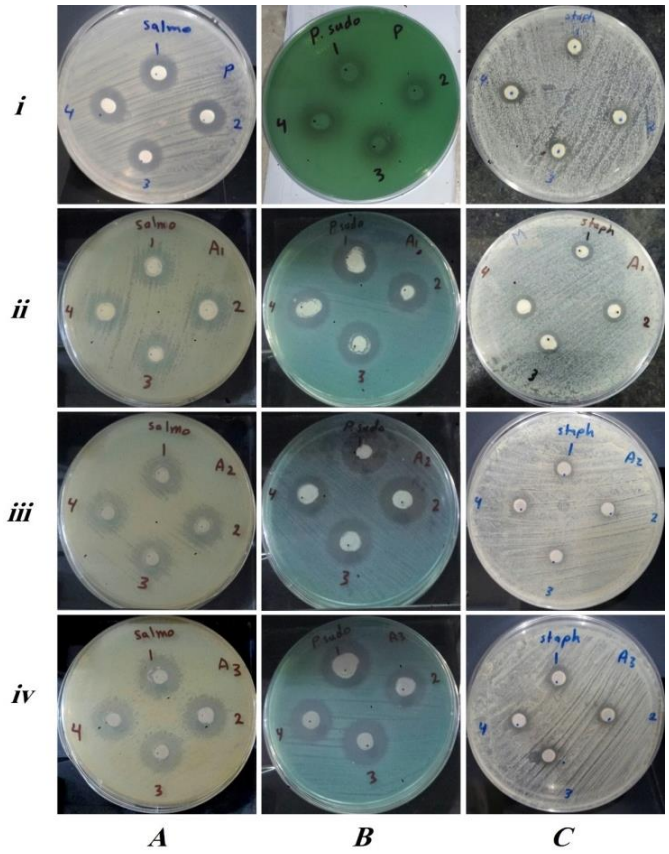

Figure 11: Illustrates the antibacterial activities of MgO-$Bi_{2-x}Ag_xO_3$ nanocomposites with varying silver doping levels against different bacterial strains. The rows represent the different samples: (i) pure, (ii) 0.3 Ag, (iii) 0.5 Ag, and (iv) 0.7 Ag, while the columns correspond to the bacterial strains: (A) *S. typhimurium,* (B) *P. aeruginosa*, and (C) *S. aureus.*

Table 5: A comparison of antibacterial analysis of MgO-$Bi_{2-x}Ag_xO_3$ nanocomposites with other nanocomposites.

Metal oxide nanocomposites	Inhibition Zone (mm)			
	Staphylococcus aureus	*S. typhimurium*	*P. aeruginosa*	Reference
MgO-$Bi_{(2-x)}Ag_xO_3$	10	20	23	Current work
ZnO–V_2O_5-WO_3	17	-	18	[78]
Co_3O_4-CuO-ZrO_2	10	-	-	[79]
CdO–ZnO–MgO	-	-	22	[80]
CuO– CeO_2–ZnO	14	-	12	[81]

4. Conclusion

In this study, MgO-$Bi_{2-x}Ag_xO_3$ nanocomposites were successfully synthesized using a simple solvent-deficient method. Structural analysis confirmed the formation of the monoclinic α-Bi_2O_3phase for all compositions, while the absence of secondary phases indicated good dispersion of MgO and silver within the Bi_2O_3 matrix. The incorporation of Ag influenced crystallite size, surface morphology, and optical behavior, with moderate Ag content producing the most noticeable improvements. Optical studies revealed a slight narrowing of the bandgap with increasing Ag concentration, which was attributed to the introduction of Ag-related electronic states. The antibacterial performance of the nanocomposites was significantly enhanced by silver doping, particularly against Gram-negative bacteria. This improvement is likely due to the combined effects of Ag ion release, reactive oxygen species generation, and increased surface interaction with bacterial cells. Overall, the results demonstrate that controlled Ag incorporation effectively tailors the multifunctional properties of MgO–Bi_2O_3-based nanocomposites. The materials synthesized in this work show promise for applications requiring enhanced antibacterial activity and tunable optical properties, especially in medical and environmental fields.

Data Availability

The datasets used and analyzed during the current study are available from the corresponding author upon reasonable request.

Funding

This research received no specific grant from any funding agency in the public, commercial, or not-for-profit sectors.

Conflict of Interest

The authors declare that there are no conflicts of interest.

References

[1] Zhang, W., Tay, H.L., Lim, S.S., Wang, Y., Zhong, Z., Xu, R. (2010) Supported cobalt oxide on MgO: highly efficient catalysts for degradation of organic dyes in dilute solutions, *Applied Catalysis B: Environmental* **95**: 93-99.

[2] Suryawanshi, S.M., Badwaik, D.S., Shinde, B.S., Gaikwad, K.D., Shkir, M., Chandekar, K.V., Gundale, S. (2023) A comprehensive study on structural, magnetic and dielectric properties of $Ni_{0.3}Cu_{0.3}Zn_{0.4}Fe_{1.8}Cr_{0.2}O_4$ nanoparticles synthesized by sol-gel auto combustion route, *Journal of Molecular Structure* **1272**: 134173.

[3] Spoto, G., Gribov, E., Ricchiardi, G., Damin, A., Scarano, D., Bordiga, S., Lamberti, C., Zecchina, A. (2004) Carbon monoxide MgO from dispersed solids to single crystals: a review and new advances, *Progress in Surface Science* **76**: 71-146.

[4] Edukondalu, A., Stalin, S., Reddy, M.S., Eke, C., Alrowaili, Z., Al-Buriahi, M. (2022) Synthesis, thermal, optical, mechanical and radiation-attenuation characteristics of borate glass system modified by Bi_2O_3/MgO, *Applied Physics A* **128**: 331.

[5] Shannon, R.D. (1976) Revised effective ionic radii and systematic studies of interatomic distances in halides and chalcogenides, *Foundations of Crystallography* **32**: 751-767.

[6] Al-Hammadi, A., Alnehia, A., Al-Sharabi, A., Alnahari ,H., Al-Odayni, A.-B. (2023) Synthesis of trimetallic oxide (Fe_2O_3–MgO–CuO) nanocomposites and evaluation of their structural and optical properties, *Scientific Reports* **13**: 12927.

[7] Richards, R., Li, W., Decker, S., Davidson, C., Koper, O., Zaikovski ,V., Volodin, A., Rieker, T., Klabunde, K.J. (2000) Consolidation of metal oxide nanocrystals. Reactive pellets with controllable pore structure that represent a new family of porous, inorganic materials, *Journal of the American Chemical Society* **122**: 4921.4925-

[8] Ren, A., Liu, C., Hong, Y., Shi, W., Lin, S., Li, P. (2014) Enhanced visible-light-driven photocatalytic activity for antibiotic degradation using magnetic $NiFe_2O_4$/Bi_2O_3 heterostructures, *Chemical Engineering Journal* **258**: 301-308.

[9] Krishnamoorthy, K., Moon, J.Y., Hyun, H.B., Cho, S.K., Kim, S.-J. (2012) Mechanistic investigation on the toxicity of MgO nanoparticles toward cancer cells, *Journal of Materials Chemistry* **22**: 24610-24617.

[10] Elashmawi, I., Menazea, A. (2025) Influence of laser ablation preparation of MgO and Bi_2O_3 nanoparticles on the optical and dielectric behavior of the PVA/PEO polymer blend, *RSC Advances* **15**: 48325-48336.

[11] Wahab, R., Ansari, S., Dar, M.A., Kim, Y.S., Shin, H.S. (2007) Synthesis of magnesium oxide nanoparticles by sol-gel process. Materials Science Forum, **558**, pp. 983-986.

[12] Tang, Z.-X., Fang, X.-J., Zhang, Z.-L., Zhou, T., Zhang, X.-Y., Shi, L.-E. (2012) Nanosize MgO as antibacterial agent: preparation and characteristics, *Brazilian Journal of Chemical Engineering* **29**: 775-781.

[13] Yan, Y., Zhou, Z., Cheng, Y., Qiu, L., Gao, C., Zhou, J. (2014) Template-free fabrication of α-and β-Bi_2O_3 hollow spheres and their visible light photocatalytic activity for water purification, *Journal of Alloys and Compounds*.108-102 :605

[14] Han, W., Xiang, W., Chen, X., Ji, Y., Meng, Z., Qiang, T., Lv, Y. (2024) Enhanced photocatalytic performance of Cr doped MgO/Bi_2O_3 nanocomposite for efficient hydroxylation of benzene to phenol under visible-light irradiation, *Chemical Physics* **577**: 112120.

[15] Bian, Z., Zhu, J., Wang, S., Cao, Y., Qian, X., Li, H. (2008) Self-assembly of active Bi_2O_3/TiO_2 visible photocatalyst with ordered mesoporous structure and highly crystallized anatase, *The Journal of Physical Chemistry C* **112**: 6.6262-258

[16] Gurunathan, K. (2004) Photocatalytic hydrogen production using transition metal ions-doped γ-Bi_2O_3 semiconductor particles, *International Journal of Hydrogen Energy* **29**: 933-940.

[17] Fan, H., Teng, X., Pan, S., Ye, C., Li, G., Zhang, L. (20 (05Optical properties of δ-Bi_2O_3 thin films grown by reactive sputtering, *Applied Physics Letters* **87**: 231916

[18] López-Salinas, F., Martínez-Castañón, G., Martínez-Mendoza, J., Ruiz, F. (2010) Synthesis and characterization of nanostructured powders of Bi_2O_3, BiOCl and Bi, *Materials Letters* **64**: 1555-1558.

[19] Takeyama, T., Takahashi, N., Nakamura, T., Ito, S. (2004) Growth of the high reflectivity Bi_2O_3 glass films by atmospheric pressure halide CVD, *Optical Materials* **26**: 413-415.

[20] Sood, S., Umar ,A., Mehta, S.K., Kansal, S.K. (2015) α-Bi_2O_3 nanorods: An efficient sunlight active photocatalyst for degradation of Rhodamine B and 2, 4, 6-trichlorophenol, *Ceramics International* **41**: 3355-3364.

[21] Bhande, S.S., Mane, R.S., Ghule, A.V., Han, S.-H. (20 (11A bismuth oxide nanoplate-based carbon dioxide gas sensor, *Scripta Materialia* **65**: 1081-1084.

[22] Gujar, T., Shinde, V., Lokhande, C., Han, S.-H. (2006) Electrosynthesis of Bi_2O_3 thin films and their use in electrochemical supercapacitors, *Journal of Power Sources* **161**: 1479-1485.

[23] Li, E.-J., Xia, K., Yin, S.-F., Dai, W.-L., Luo, S.-L., Au, C.-T. (2011) Preparation, characterization and photocatalytic activity of Bi_2O_3–MgO composites, *Materials Chemistry and Physics* **125**: 236-241.

[24] Wachsman, E.D ,.Lee, K.T. (2011) Lowering the temperature of solid oxide fuel cells, *Science* **334**: 935-939.

[25] Hernandez-Delgadillo, R., Velasco-Arias, D., Martinez-Sanmiguel, J.J., Diaz, D., Zumeta-Dube, I., Arevalo-Niño, K., Cabral-Romero, C. (2013) Bismuth oxide aqueous colloidal nanoparticles inhibit Candida

albicans growth and biofilm formation, *International Journal of Nanomedicine* **8**: 1645-1652.

[26] Qin, F., Zhao, H., Li, G., Yang, H., Li, J., Wang, R., Liu, Y., Hu, J., Sun, H., Chen, R. (2014) Size-tunable fabrication of multifunctional Bi_2O_3 porous nanospheres for photocatalysis, bacteria inactivation and template-synthesis, *Nanoscale* **6**: 5402-5409.

[27] Riente, P., Matas Adams, A., Albero, J., Palomares, E., Pericàs, M.A. (2014) Light-driven organocatalysis using inexpensive, nontoxic Bi_2O_3 as the photocatalyst, *Angewandte Chemie International Edition* **53**: 9613-9616.

[28] Li, L., Yan, B. (2009) CeO2–Bi_2O_3 nanocomposite: two step synthesis, microstructure and photocatalytic activity, *Journal of Non-Crystalline Solids* **355**: 776-779.

[29] Jan, T., Azmat, S., Wahid, B., Adil, M., Alawadhi, H., Mansoor, Q., Farooq, Z., Ilyas, S., Ahmad, I., Ismail, M. (2018) Chemically synthesized ZnO-Bi_2O_3 (BZO) nanocomposites with tunable optical, photoluminescence and antibacterial characteristics, *Materials Science in Semiconductor Processing* **84**: 71-75.

[30] Feng, Q.L., Wu, J., Chen, G.-Q., Cui, F.-Z., Kim, T., Kim, J. (2000) A mechanistic study of the antibacterial effect of silver ions on *Escherichia coli* and *Staphylococcus aureus*, *Journal of Biomedical Materials Research* **52**: 662-668.

[31] Pal, S., Tak, Y.K., Song, J.M. (2007) Does the antibacterial activity of silver nanoparticles depend on the shape of the nanoparticle? A study of the gram-negative bacterium *Escherichia coli*, *Applied and Environmental Microbiology* **73**: 1712-1720.

[32] Koga, H., Kitaoka, T., Wariishi, H. (2009) *In situ* synthesis of silver nanoparticles on zinc oxide whiskers incorporated in a paper matrix for antibacterial applications, *Journal of Materials Chemistry* **19**: 2135-2140.

[33] Aziz, A., Khalid, M., Akhtar, M.S., Nadeem, M., Gilani, Z., Hmn, U.H.K.A., Rehman, J., Ullah, Z., Saleem, M. (2018) Structural, Morphological and Optical Investigations of Silver Nanoparticles Synthesized by Sol-Gel Auto-Combustion Method, *Digest Journal of Nanomaterials & Biostructures* **13**: 615 - 623.

[34] Capek, I. (2004) Preparation of metal nanoparticles in water-in-oil (w/o) microemulsions, *Advances in Colloid and Interface Science* **110**: 49-74.

[35] Al-Sharabi, A., Sada'a ,K.S., Al-Osta, A., Abd-Shukor, R. (2022) Structure, optical properties and antimicrobial activities of MgO–$Bi_{2-x}Cr_xO_3$ nanocomposites prepared via solvent-deficient method, *Scientific Reports* **12**: 10647.

[36] Raza, W., Haque, M., Muneer, M., Harada, T., Matsumura, M. (2015) Synthesis, characterization and photocatalytic performance of visible light induced bismuth oxide nanoparticle, *Journal of Alloys and Compounds* **648**: 641-650.

[37] Georgekutty, R., Seery, M.K., Pillai, S.C. (2008) A highly efficient Ag-ZnO photocatalyst: synthesis, properties, and mechanism, *The Journal of Physical Chemistry C* **112**: 13563-13570.

[38] Yıldırım, Ö.A., Unalan, H.E., Durucan, C. (2013) Highly efficient room temperature synthesis of silver-doped zinc oxide (ZnO: Ag) nanoparticles: structural, optical, and photocatalytic properties, *Journal of the American Ceramic Society* **96**: 766-773.

[39] Cai, Y., Wu, D., Zhu, X., Wang, W., Tan, F., Chen, J., Qiao, X., Qiu, X. (2017) Sol-gel preparation of Ag-doped MgO nanoparticles with high efficiency for bacterial inactivation, *Ceramics International* **43**: 1066-1072.

[40] Jeejamol, D., Raj, A.M.E., Jayakumari, K., Ravidhas, C. (2018) Optimization of CdO nanoparticles by Zr^{4+} doping for better photocatalytic activity, *Journal of Materials Science: Materials in Electronics* **29**: 97-116.

[41] Alnehia, A., Al-Sharabi, A., AL-Osta, A. (2023) Effect of Cu^{2+} and Cr^{3+} doping on structural, morphological, optical and electrical properties of zinc sulfide nanoparticles for optoelectronic applications, *Journal of Materials Science: Materials in Electronics* **34**: 2004.

[42] Shkir, M., Khan, A., Chandekar, K.V., Sayed, M., El-Toni, A.M., Ansari, A.A., Adil, S.F., Ghaithan, H., Algarni, H., AlFaify, S. (2021) Dielectric and electrical properties of La@ NiO SNPs for high-performance optoelectronic applications, *Ceramics International* **47**: 15611-15621.

[43] Mohanraj, K., Balasubramanian, D., Chandrasekaran, J., Bose, A.C. (2018) Synthesis and characterizations of Ag-doped CdO nanoparticles for PN junction diode application, *Materials Science in Semiconductor Processing* **79**: 74-91.

[44] Iljinas, A., Marcinauskas, L. (2015) Formation of bismuth oxide nanostructures by reactive plasma assisted thermal evaporation, *Thin Solid Films* **594**: 192-196.

[45] Zhang, J., Han, Q ,.Wang, X., Zhu, J., Duan, G. (2016) Synthesis of δ-Bi_2O_3 microflowers and nanosheets using CH_3COO (BiO) self-sacrifice precursor, *Materials Letters* **162**: 218-221.

[46] Pan, R., Wu, Y., Wang, Q., Hong, Y. (2009) Preparation and catalytic properties of platinum dioxide nanoparticles: A comparison between conventional heating and microwave-assisted method, *Chemical Engineering Journal* **153**: 206-210.

[47] Sonkusare, V.N., Chaudhary, R.G., Bhusari, G.S., Rai, A.R., Juneja, H.D. (2018) Microwave-mediated synthesis, photocatalytic degradation and antibacterial activity of α-Bi_2O_3 microflowers/novel γ-Bi_2O_3 microspindles, *Nano-Structures & Nano-Objects* **13**: 121-131.

[48] Al-Douri, A., Al-Shakily, F., Alias, M., Alnajjar, A. (2010) Optical Properties of Al-and Sb-Doped CdTe Thin Films, *Advances in Condensed Matter Physics* **2010**: 947684.

[49] Dahshan, M. (2002) Introduction to Material Science and engineering, 2nd ed., *McGraw Hill*, New York, USA, pp. 370

[50] Chen, Y., Tse, W.H., Chen, L., Zhang, J. (2015) Ag nanoparticles-decorated ZnO nanorod array on a mechanical flexible substrate with enhanced optical and antimicrobial properties, *Nanoscale Research Letters* **10**: 106.

[51] Al-Sharabi, A., Alnehia, A., Ahmed, A.-O., Yahya, N.A. (2019) Effect of copper doping on structural and optical properties of zinc sulfide (ZnS) nanoparticles, *Albaydha University Journal* **1**: 224-234.

[52]Chau, J.L.H., Lin, Y.-M., Li, A.-K., Su, W.-F., Chang, K.-S., Hsu, S.L.-C., Li, T.-L. (2007) Transparent high refractive index nanocomposite thin films, *Materials Letters* **61**: 2908-2910.

[53] Indolia, A.P., Gaur, M. (2013) Optical properties of solution grown PVDF-ZnO nanocomposite thin films, *Journal of Polymer Research* **20**: 43.

[54] Al-Sharabi, A., Ahmed, A.-O., Alnehia, A., Al-Odayni, A.-B (2023) . Chromium and copper dual-doped zinc sulfide nanoparticles: Synthesis, structural, morphological and optical properties, *Results in Optics* **13**: 100534.

[55] Al-Sharabi, A., Al-Hussam, A.M., Abdullh, S.K. (2019) Synthesis and characterization of metal complexes of Cu (ii) and Cd (ii) with poly vinyl alcohol and studied of electrical and optical properties, *International Journal of Multidisciplinary Research and Development* **6**: 19-26.

[56] Husain, S., Alkhtaby, L.A., Giorgetti, E., Zoppi, A., Miranda, M.M. (2014) Effect of Mn doping on structural and optical properties of sol gel derived ZnO nanoparticles, *Journal of Luminescence* **145**: 132-137.

[57] Thomas, M., Cui, J. (2010) Electrochemical route to p-type doping of ZnO nanowires, *The Journal of Physical Chemistry Letters* **1**: 1090-1094.

[58] Gupta, M.K., Sinha, N., Kumar, B. (2011) p-type K-doped ZnO nanorods for optoelectronic applications, *Journal of Applied Physics* **109**: 083532

[59] Trabelsi, A.B.G., Chandekar, K.V., Alkallas, F.H., Ashraf, I., Hakami ,J., Shkir, M., Kaushik, A., AlFaify, S. (2022) A comprehensive study on Co-doped CdS nanostructured films fit for optoelectronic applications, *Journal of Materials Research and Technology* **21**: 3982-4001.

[60] Chitte, H.K., Bhat, N.V., Karmakar, N.S., Kothari, D.C., Shinde, G.N. (2012) Synthesis and characterization of polymeric composites embeded with silver nanoparticles, *World Journal of Nano Science and Engineering* **2**: 19-24.

[61] Mansour, A., Mansour, S., Abdo, M. (2015) Improvement structural and optical properties of ZnO/PVA nanocomposites, *IOSR Journal of Applied Physics* **7**: 60-69.

[62] Kadham, A.J., Hassan, D., Mohammad, N., Ah-yasari, A.H. (2018) Fabrication of (polymer blend-magnesium oxide) nanoparticle and studying their optical properties for optoelectronic applications, *Bulletin of Electrical Engineering and Informatics* **7**: 28-34.

[63] Chandekar, K.V., Shkir, M., Khan, A., Sayed, M., Alotaibi, N., Alshahrani, T., Algarni, H., AlFaify, S. (2021) Significant and systematic impact of yttrium doping on physical properties of nickel oxide nanoparticles for optoelectronics applications, *Journal of Materials Research and Technology* **15**: 2584-2600.

[64] Shkir, M., Chandekar, K.V., Khan, A., Alshahrani, T., El-Toni, A.M., Sayed, M., Singh, A., Ansari, A.A., Muthumareeswaran, M., Aldalbahi, A. (2021) Tailoring the structure-morphology-vibrational-optical-dielectric and electrical characteristics of Ce@ NiO NPs produced by

facile combustion route for optoelectronics, *Materials Science in Semiconductor Processing* **126**: 105647.

[65] Alsalmah, H.A. (2024) Structural, thermal, optical, morphological, electrical, and photocatalytic characteristics of silver-doped bismuth oxide synthesized by the green route, *Ceramics International* **50**: 14675-14685.

[66] Th, S., Sharma, J., Sanjay, K. (2017) Effect of Silver Doping on Properties of ZnO nanoparticles by chemical Precipitation method, *International Journal of Engineering Technology Science and Research* **4**: 112.

[67] Arakha, M., Saleem, M., Mallick, B., Jha, S (2015) .The effects of interfacial potential on antimicrobial propensity of ZnO nanoparticle, *Scientific Reports* **5**: 9578

[68] El-Sayyad, G.S., Mosallam, F.M., El-Batal, A.I. (2018) One-pot green synthesis of magnesium oxide nanoparticles using Penicillium chrysogenum melanin pigment and gamma rays with antimicrobial activity against multidrug-resistant microbes, *Advanced Powder Technology* **29**: 2616-2625.

[69] El-Batal, A.I., Al-Hazmi, N.E., Mosallam, F.M., El-Sayyad, G.S. (2018) Biogenic synthesis of copper nanoparticles by natural polysaccharides and Pleurotus ostreatus fermented fenugreek using gamma rays with antioxidant and antimicrobial potential towards some wound pathogens, *Microbial Pathogenesis* **118**: 159-169.

[70] He, Y., Ingudam, S., Reed, S., Gehring ,A., Strobaugh Jr, T.P., Irwin, P. (2016) Study on the mechanism of antibacterial action of magnesium oxide nanoparticles against foodborne pathogens, *Journal of Nanobiotechnology* **14**: 54.

[71] Alnehia, A., Al-Sharabi, A., Al-Odayni, A.-B., Al-Hammadi, A ,.Al-Ostoot, F.H., Saeed, W.S., Abduh, N.A., Alrahlah, A. (2023) Lepidium sativum Seed Extract-Mediated Synthesis of Zinc Oxide Nanoparticles: Structural, Morphological, Optical, Hemolysis, and Antibacterial Studies, *Bioinorganic Chemistry and Applications*.4166128 :2023

[72] Verma, S.K., Jha, E., Panda, P.K., Das, J.K., Thirumurugan, A., Suar, M., Parashar, S. (2018) Molecular aspects of core-shell intrinsic defect induced enhanced antibacterial activity of ZnO nanocrystals, *Nanomedicine* **13**: 43-68.

[73] Xia, T., Kovochich, M., Liong, M., Madler, L., Gilbert, B., Shi, H., Yeh, J.I., Zink, J.I., Nel, A.E. (2008) Comparison of the mechanism of toxicity of zinc oxide and cerium oxide nanoparticles based on dissolution and oxidative stress properties, *ACS Nano*.2134-2121 :2

[74] Karthik, K., Dhanuskodi, S., Gobinath, C., Prabukumar, S., Sivaramakrishnan, S. (2018) Multifunctional properties of microwave assisted CdO–NiO–ZnO mixed metal oxide nanocomposite: enhanced photocatalytic and antibacterial activities, *Journal of Materials Science: Materials in Electronics* **29**: 5459-5471.

[75] Alnehia, A., Hadi, M., Alnahari, H., Al-Sharabi, A. (2024) Optical, structural and antibacterial properties of phase heterostructured Fe_2O_3–CuO–$CuFe_2O_4$ nanocomposite, *Scientific Reports* **14**: 14392.

[76] Al-Odayni, A.-B., Alnehia, A., Al-Sharabi, A., Al-Hammadi, A., Saeed, W.S., Abduh, N.A. (2023) Biofabrication of Mg-doped ZnO nanostructures for hemolysis and antibacterial properties, *Bioprocess and Biosystems Engineering* **46**: 1817-18.24

[77] Alnehia, A., Alnahari, H., Al-Sharabi, A. (2024) Characterization and antibacterial activity of MgO/CuO/Cu_2MgO_3 nanocomposite synthesized by sol-gel technique, *Results in Chemistry* **8**: 101620.

[78] Mukhtar, F., Munawar, T., Nadeem, M.S., Rehman, M.N.u., Riaz, M., Iqbal, F. (2021) Dual S-scheme heterojunction ZnO–V_2O_5–WO nanocomposite with enhanced photocatalytic and antimicrobial activity, *Materials Chemistry and Physics* **263**: 124372.

[79] Hadi, M. (2024) Co_3O_4-CuO-ZrO_2 Nanocomposite: Optical, spectral, morphological, structural and antibacterial studies, *Results in Chemistry* **7**: 101311.

[80] Revathi, V., Karthik, K. (2018) Microwave assisted CdO–ZnO–MgO nanocomposite and its photocatalytic and antibacterial studies, *Materials Science: Materials in Electronics* **29** 18519–18530.

[81] Subhan, M.A., Uddin, N., Sarker, P., Azad, A.K., Begum, K. (2015) Photoluminescence,photocatalytic and antibacterial activities of CeO_2-CuO-ZnO nanocomposite fabricated by co-precipitation method, *Spectrochimica Acta Part A* **149** 839–850.